

Article title

Christian Neureuter, Author Name² and Author Name^{1,2}

¹ Department One, Institution One, City One, Country One

² Department Two, Institution Two, City Two, Country Two

E-mail: xxx@xxx.xx

Received xxxxxx

Accepted for publication xxxxxx

Published xxxxxx

Abstract

Sample text inserted for illustration. Replace with abstract text. Your abstract should give readers a brief summary of your article. It should concisely describe the contents of your article, and include key terms. It should be informative, accessible and not only indicate the general scope of the article but also state the main results obtained and conclusions drawn. The abstract should be complete in itself; it should not contain undefined abbreviations and no table numbers, figure numbers, references or equations should be referred to. It should be suitable for direct inclusion in abstracting services and should not normally be more than 300 words.

Keywords: term, term, term

1. Introduction

For problems which can be described by linear systems of differential equations, the adjoint method can be used to calculate the gradient. The adjoint method involves defining an equivalent, linear, adjoint system which we can use with linear algebra relations to derive an easily calculable gradient using only one forward and one adjoint simulation.

Typical inverse design algorithms utilize methods such as numerical “finite difference” (FD) differentiation, which is a two point approximation of the gradient vector. These FD optimizations require the perturbation of each parameter, simulated independently. Hence, the number of simulations needed scales with the number of parameters. With the adjoint method, though, we avoid this pitfall because only one forward and one adjoint simulation are needed. Since the simulation of the fields is computationally expensive, the adjoint method offers an orders-of-magnitude improvement in computation time over traditional FD optimization methods.

Lalau-Keraly et. al. showed, in 2013, that the adjoint method could be used to accurately calculate the gradient for photonic system optimization [2]. The adjoint method has been gaining popularity ever since; being used to design

optical gratings, multiplexing waveguides, and other, non-linear nano-photonics devices [3, 4, 5]. It has, even more recently, been suggested as a method for dielectric laser acceleration (DLA) [Add these references here: <https://doi.org/10.1103/PhysRevLett.111.134803>, [16] = <https://doi.org/10.1038/nature12664>, 20,21, <https://doi.org/10.1364/AOP.461142>] structure optimization [6, 1]. This is ideal for designing complex ‘on-chip’ photonic DLA structures [5]. Inverse-design DLA-related research up to this point has, however, assumed periodic grating structures. The periodicity, however, is dependent on the electron velocity – which grows as the electron accelerates. Therefore, long structures would require compensation for the inevitable dephasing of the particle versus the accelerating field. Here, we extend adjoint inverse design to accelerating, non-periodic structures for phase-matched nanophotonic particle acceleration by extending the adjoint method. We also introduce a custom optimizer necessary for bound-constrained, non-convex adjoint optimization.

Conventional high energy particle acceleration is done via RF waves and metallic cavities [9]. In contrast, recent advances in ultra-fast optics made commercially available femtosecond laser sources with high peak field intensities. These ultra-short pulses have been demonstrated in DLAs to

provide a maximum acceleration gradient of >1 GeV/m and field strengths up to 9 GV/m [11], far higher than a typical RF linear accelerator (linac) [12, 13], which is usually operated at field strengths in the 25-50 MV/m range.

DLA involves using a dielectric material, in our case silicon, to diffract the incoming laser light and use the near fields to accelerate a charged particle. Although the idea for dual grating, dual driven, DLAs has been around for quite some time [14], it wasn't until the last decade that they were successfully tested and research consequently pursued. It took nano-fabrication advancements to facilitate the interplay of infra-red lasers and DLAs: due to the wavelength of the applied field, and considering subrelativistic electrons, structure features are sub-micron. The benefits of dielectric materials over metals is the increased damage threshold, which allows access to higher acceleration gradients compared to RF accelerators [20], and thus about two orders of magnitude smaller accelerators.

Today, the nanophotonic DLA architecture mainly utilizes the dual-pillar colonnade geometry [Palmer “open accelerating structures” 1986] [22] [https://doi.org/10.1016/j.nima.2018.01.065], which can vary in both design and optical drive [https://doi.org/10.1364/AOP.461142]. Generally, a symmetric arrangement of pillar pairs is used, which provides a cosine-hyperbolic accelerating field. Uniformity of the accelerating field, within a given period, is necessary for DLAs, in order to minimize the unwanted deflection effects and enable longer accelerators [22]. Moreover, dual sided laser illumination can provide perfect field symmetry and, for simplicity, is the setup used in our simulations.

Outline paper

2. Background

2.1. Adjoint method

For problems described by linear systems of differential equations, the adjoint method can be used to calculate the gradient [2, 3]. In the adjoint method, the problem is arranged in a form of

$$A(\phi)x = b$$

1

where A is a sparse matrix dependent on the parameters $\vec{\phi}$ describing the system and b is some ‘driving source’. From this we can define a complex objective function $J = J(x)$, which similarly depends on our complex fields x . If we rearrange Eq. 1 and then differentiate with respect to ϕ , we get

$$\text{sdfasd} (2.2)2$$

If we similarly differentiate the objective function J with respect to ϕ , we get

$$(2.3)3$$

where the factor of 2 comes out from x being complex-valued.

If A is symmetric, we can define a second, symmetric, adjoint system.

$$(2.4)4$$

Since, $A^T = A$, the adjoint solution can be rearranged as

$$(2.5)5$$

We can see then, from Eqs. 2.3 and 2.5 that

$$(2.6)6$$

Thus giving us a relation between the change in the objective function and the field solution, as function of the parameter set $\vec{\phi}$. In the next section, we will relate this result to the electromagnetic nanophotonic field solution.

2.2. Adjoint method for DLA

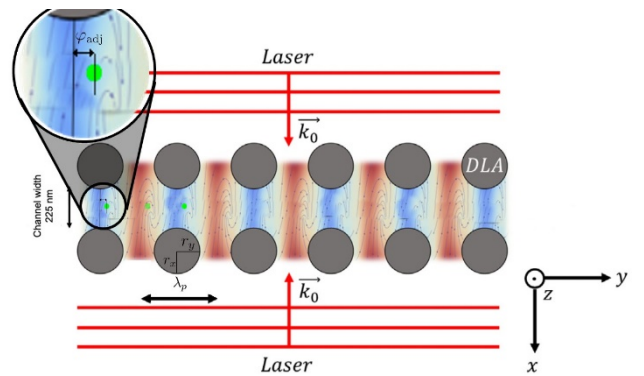


Figure 2.1: Dual Grating, Dual Drive, DLA structure with corresponding variable definitions. Figure edited from [24] to match our definitions.

The electromagnetic solution of Maxwell's equations in the frequency domain can be used to describe photonic systems for the adjoint method:

$$(2.7)7$$

where $J(\vec{r})$ is the electric current distribution, k_l is the wave vector of the laser, ϵ_r is the relative permittivity, and for non magnetic materials, the susceptibility $\mu = \mu_0$.

Since we seek to maximize the acceleration gradient which is the amount of energy gain per unit length, we need to know this gradient over one optical period. In a typical DLA we can write this as

$$G = \frac{1}{T} \int_0^T E_{\parallel}(\vec{r}(t), t) dt \quad 8$$

$$(2.8)$$

where E_{\parallel} is the projection of the incident field on the particle's trajectory, sampled at $\vec{r}(t)$.

Since we are working in two dimension; with an incident laser with frequency ω , the fields are of the form

$$E(\vec{r}, t) = \Re \tilde{E}(\vec{r}) e^{i\omega t} \quad 9$$

where \tilde{E} is the complex valued electric field. Here we use monochromatic beams, however, the next step would be to generalize this to broadband light.

Our 'test' particle is set to move along the line $x = 0$, with velocity $\vec{v} = \beta c \hat{y}$, where c is the speed of light in vacuum and $0 < \beta \leq 1$. The particle's position is then given by, $y(t) = y_0 + \beta ct$

For an infinitely long structure (or $T \rightarrow \infty$), our acceleration gradient can be interpreted as being an integral over one spatial period. With our synchronicity condition, we can rewrite Eq. [acceleration gradient] as

$$G = \frac{1}{\lambda_p} \Re e^{i\varphi_{\text{adj}}} \int_0^{\lambda_p} \tilde{E}_y(0, y) e^{i\frac{2\pi}{\lambda_p} y} dy \quad 10$$

where $\varphi_{\text{adj}} = 2\pi y_0/\lambda_p$ is the *adjoint phase*—also referred to as the 'injection phase'—which is the relative phase of the particle with the oscillation of the incident field, as it enters the cell.

Then the acceleration gradient can be described by an inner product of the forward and adjoint fields.

$$G = \Re \langle \vec{E}, \vec{\eta} \rangle \quad 11$$

where we can see from Eq. [relative acceleration gradient integral], η is defined as

$$\vec{\eta}(x, y) = \frac{1}{\lambda_p} e^{i\frac{2\pi}{\lambda_p} y} \delta(x) \hat{y} \quad 12$$

2.3. Adjoint source

In order to calculate the gradient of this cost function, we need to fully define our adjoint source. Since we have a charged particle moving, it makes sense to think of the adjoint source as a current. This radiating current density can be described by

$$\vec{J}_{\text{rad}}(x, y; t) = q \beta c \delta(x) \delta(y - y_0 - c\beta t) \hat{y} \quad \text{\label{adjoint current density}} \quad 13$$

Fourier transforming Eq. [adjoint current density]¹

$$\begin{aligned} \vec{J}_{\text{rad}}(x, y; \omega_l) &= q \beta c \delta(x) \hat{y} \int_{-\infty}^{\infty} e^{i\omega_l t} \delta(y - y_0 - c\beta t) dt \\ &= q e^{i\frac{\omega_l(y-y_0)}{c\beta}} \delta(x) \hat{y} \\ &= q e^{i\frac{2\pi}{\beta\lambda} y} e^{-i\varphi_{\text{adj}}} \delta(x) \hat{y} \end{aligned} \quad 14$$

where again, $\varphi_{\text{adj}} = 2\pi y_0/\lambda_p$ is the *adjoint/injection* phase. From Eqs. [Maxwell frequency domain] and [eta definition], we see that our adjoint source for Maxwell's equations can be defined in terms of our adjoint field (η) as

$$\vec{J}_{\text{adj}} = \frac{-i}{\mu_0 \omega_l} \vec{\eta} \quad 15$$

From this, we can see that

$$\vec{J}_{\text{adj}} = \frac{-ie^{i\varphi_{\text{adj}}}}{2\pi\mu_0\omega_l q} \vec{J}_{\text{rad}} \quad 16$$

enlightening us that the adjoint field E_{adj} corresponds (up to a complex constant) to the field radiating from a particle traversing the accelerator. What this means for us is that we must simulate our structure as an accelerator ($A\vec{E} = -i\omega\mu_0\vec{J}_{\text{acc}}$) and a radiator ($A\vec{E}_{\text{adj}} = -i\omega\mu_0\vec{J}_{\text{adj}}$).

In simulations, we can model our adjoint source, then, as a plane wave with a y varying phase. From Eqs. [eta definition] and [adjoint source field eta definition], the phase envelope of

¹ Forward Fourier transform $H(\omega) = \mathcal{F}(h(t)) = \int_{-\infty}^{\infty} f(t) e^{i\omega t} dt$ Inverse Fourier transform $h(t) = \mathcal{F}^{-1}(H(\omega)) = \frac{1}{2\pi} \int_{-\infty}^{\infty} \mathcal{F}(t) e^{-i\omega t} dy$

the adjoint source can be defined, up to a complex constant, by

$$E_{y_{\text{adj}}}(y) = e^{i2\pi\left(\frac{y+\lambda_p/2}{\lambda_p}\right)} \quad 17$$

where we have used $\frac{y+\lambda_p/2}{\lambda_p}$ to ensure that our spatial period is centered within the cell. The phase of this source is determined by the periodicity of the structure λ_p .

To change the relative phase between the particle and field, we look at Eqs. [\[cost function definition\]](#) and [\[adjoint source as radiator\]](#) and see that we can either change the adjoint phase ϕ_{adj} or the phase of the first harmonic ϕ_{e_1} . In a multi-cell structure, we need to remember to specify that this will be the *injection* phase, and thus we will specifically need to change $\phi_{e_{1_1}}$ (the phase of the first harmonic of the **first** cell). Since we defined the adjoint phase as the phase difference between the incident laser and the injection of the particle into the structure, we can simply adjust the phase of the source by adding a constant shift to the exponential in Eq. [\[adjoint source envelope\]](#).

$$E_{y_{\text{adj}}} = e^{i2\pi\left(\frac{y+\lambda_p/2}{\lambda_p}\right) + i\phi_{\text{adj}}} \quad 18$$

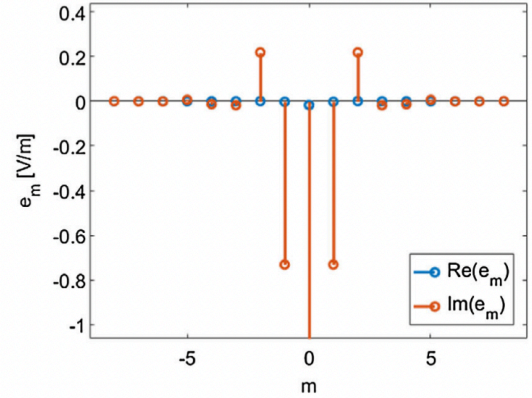
For periodic structures, one can also shift the entire adjoint source; since it depends on y , changing y will introduce a relative phase shift. We may also change the phase of the first harmonic, which will introduce a phase offset. The y_{pos} of the pillar within its (semi-)periodic ‘cell’ principally shifts the fields along the y -axis. This will shift the relative phase between the particle’s trajectory and the phase of the fields in a given cell.

We then define our adjoint source from Eq. [\[dJ wrt the adjoint field\]](#) as

$$x_{\text{adj}}^T = C_0 E_{y_{\text{adj}}} = C_0 e^{i2\pi\left(\frac{y+\lambda_p/2}{\lambda_p}\right) + i\phi_{\text{adj}}} \quad 19$$

where C_0 is a constant, complex, scaling factor.

2.4. Forward Field & Cost Function



Plot of the of spatial harmonics in a DLA structure. Reprinted from

In order to calculate the mathematical gradient from the aforementioned adjoint method, we must define a cost function $J(x)$ which also depends on the fields x . Since we seek to maximize the acceleration gradient, it is only natural for us to call our cost function G . In order to derive G , we define our coordinate system as noted in Fig. 2.1, where the electron propagates in y and the y -polarized laser counter-propagates in the $+x$ and $-x$ directions.

The field near the gratings can be described by a Fourier series of all spatial harmonics.

$$E_y(x, y, z) = \sum_{m=-\infty}^{\infty} e_m(x, y) e^{-im\frac{2\pi}{\lambda_p}y} \quad 20$$

$$e_m(x, y) = \frac{1}{\lambda_p} \int_{-\lambda_p/2}^{\lambda_p/2} E_y(x, y, z) e^{im\frac{2\pi}{\lambda_p}y} dy \quad 21$$

with m the number of the harmonic and λ_p the period of the structure in the y -direction (the synchronicity condition). Fig. 2.2 shows the electric field’s spatial Fourier coefficients. We can see that it has a strong first harmonic and a much weaker second harmonic that is out of phase with it. So, for the purpose of maximizing the acceleration gradient, we choose to optimize only for the first harmonic. We can then define our forward field from Eq. [\[dJ wrt the adjoint field\]](#) as

$$x = e_1(0, y) \cdot e^{-i\frac{2\pi}{\lambda_p}y} \quad 22$$

Selecting only the first harmonic, $m = 1$, (hereon omitting it from equations) we can plug Eq. [\[E_y fourier series\]](#) and Eq. [\[eta definition\]](#) into Eq. [\[inner product G\]](#) and get our objective function

$$G = \frac{1}{\lambda_p x} \Re \int_0^{\lambda_p} \int_{-x/2}^{x/2} e^{i\varphi_{\text{adj}}} e_1(x, y) e^{-i\frac{2\pi}{\lambda_p} y} \cdot e^{i\frac{2\pi}{\lambda_p} y} \delta(x) dx dy \quad 23$$

Where the λ_p is discrete based on the design curve, and Λ_p is ‘continuous’ based on the particle’s trajectory, and S is the simulation region. When we assume no intra-periodic dephasing ($\lambda_p = \Lambda_p$) this simplifies to

$$G = \Re \langle e_1 \cdot e^{i\varphi_{\text{adj}}} \rangle = |e_1| \cos(\varphi_{\text{adj}} + \phi_{e_1}) \quad 24$$

Since optimization methods generally require a scalar value to optimize, and our goal is to control the acceleration gradient of a multi-period structure, it is only natural to use a least square function. This gives us our final cost value that was optimized in this paper.

$$\mathbf{G} = \sum_n (G_n - d_n)^2 \quad 25$$

where G_n is the value of the single-pillar objective function of the n -th cell and d_n is the value of the design curve for this cell. This function is then minimized, so that the curve of the G_n -values follow the design curve as closely as possible. (Eq. [cost function definition]) then becomes $G_n = \Re \langle e_{1n} \cdot e^{i\varphi_{\text{adj}}} \rangle$ and \mathbf{G} is reserved for our total, scalar cost function, defined in Eq. [multi pillar cost function].)

3. Adjoint Inverse Design

Now, we will detail how to use the adjoint method and inverse design, in our specific case of dual pillar DLA structures. Eq. [differentiated objective function J] provides us with a formula for the gradient of a cost function in the adjoint method. Using our cost function G (Eq. [cost function definition]), we know the forward and adjoint fields from Eq. [dJ wrt the adjoint field], in their respective forms from Eqs. [harmonics integral] and [eta definition]. The only thing then, that we need to calculate to be able to find the gradient of our cost function is $\frac{\partial}{\partial \mathbf{A}} \{ \mathbf{A} \} \cdot \mathbf{\Phi}$. Since our structure features are dual pillars made of silicon, as discussed in Section 2.1.1, we use a grid of ε_r to describe the system. Our parameters $\vec{\phi}$ are now the pillar radii (r_x and r_y) and their position within their cell (y). Our matrix then becomes $A(\vec{r}) \rightarrow A(\varepsilon_r(\vec{r}))$, hence

$$\frac{\partial}{\partial \mathbf{A}} \{ A(\vec{r}) \} \cdot \mathbf{\Phi} = \frac{\partial}{\partial \mathbf{A}} \{ A(\vec{r}) \} \cdot \frac{\partial}{\partial \mathbf{A}} \{ \varepsilon_r(\vec{r}) \} \cdot \mathbf{\Phi} \quad \text{\label{dA dphi}} \quad 26$$

Comparing this to Eq. [Maxwell frequency domain], we see that

$$\frac{\partial}{\partial \mathbf{A}} \{ A(\vec{r}) \} \cdot \frac{\partial}{\partial \mathbf{A}} \{ \varepsilon_r(\vec{r}) \} = -k_l^2 \quad \text{\label{dA deps}} \quad 27$$

For $\frac{\partial}{\partial \mathbf{A}} \{ \varepsilon_r(\vec{r}) \} \cdot \mathbf{\Phi}$, we can use a simple two point derivative

$$\frac{\partial}{\partial \mathbf{A}} \{ \varepsilon_r(\vec{r}) \} \cdot \mathbf{\Phi} = \frac{\Delta \varepsilon_r(\vec{r}) \cdot \mathbf{\Phi}}{\Delta \mathbf{A}} \quad \text{\label{deps dphi}} \quad 28$$

finally yielding

$$\frac{\partial}{\partial \mathbf{A}} \{ A(\vec{r}) \} \cdot \mathbf{\Phi} = -k_l^2 \frac{\Delta \varepsilon_r(\vec{r}) \cdot \mathbf{\Phi}}{\Delta \mathbf{A}} \quad \text{\label{delta epsilon delta phi}} \quad 29$$

which comprise the entries of a symmetric matrix. Earlier we made the assumption that the system was symmetric. However, as we can see in Fig. 4.1, the parameter space is neither linearly independent, nor symmetric.

Here is where we make our two primary modifications to the adjoint method. We know that our parameter space can be described by a square matrix $\mathbf{\Phi} \times \mathbf{\Phi}$, where each entry is itself an array of the relative permittivity for the simulation region. Since the space is not linearly independent, there will be intra-periodic interactions between parameters, and inter-periodic interactions between cells. This is where our second modification has to be made. These interactions require us to find the derivative as

$$\frac{\partial}{\partial \mathbf{A}} \{ A(\vec{r}) \} \cdot \mathbf{\Phi} = -k_l^2 \begin{pmatrix} \partial_{\phi_1} & \dots & \partial_{\phi_n} \\ \vdots & \ddots & \vdots \\ \partial_{\phi_1} & \dots & \partial_{\phi_n} \end{pmatrix} \cdot \begin{pmatrix} 1 & \dots & 1 \\ \vdots & \ddots & \vdots \\ 1 & \dots & 1 \end{pmatrix} = \begin{pmatrix} \partial_{\phi_1} \varepsilon_r + \dots \\ \partial_{\phi_n} \varepsilon_r + \dots \\ \partial_{\phi_1} \varepsilon_r + \dots \end{pmatrix} \quad \text{\label{1 pillar epsilon matrix}} \quad 30$$

Where we see that the sum of each column, with the differentials distributed, is the gradient for each respective parameter. To account for the interactions, though, we must apply a ‘filter’ to each column. This filter is a Gaussian with a variance of 1 laser wavelength, which is done because we treat our system in the semi-classical limit, at which, Huygen’s principle tells us that each point on a diffracted wavefront is itself a point source that is described by a Dirac delta function, which can be numerically approximated by a Gaussian curve with a variance of λ . After applying the rolling filter,

according to λ_{p_n} , we sum each column and obtain the approximate differential for each parameter.

$$(\partial_{r_{x_1}}, \partial_{r_{y_1}}, \partial_{r_{x_2}}, \partial_{r_{y_2}}, \partial_{r_{x_3}}, \partial_{r_{y_3}}) \varepsilon_r \cdot \begin{pmatrix} \begin{pmatrix} 1 & 0.6 \\ 0.6 & 1 \end{pmatrix} & \begin{pmatrix} 0.2 & 0.05 \\ 0.05 & 0.2 \end{pmatrix} & \begin{pmatrix} 0.01 & 0 \\ 0 & 0.01 \end{pmatrix} \\ \begin{pmatrix} 1 & . \\ . & 1 \end{pmatrix} & \begin{pmatrix} . & . \\ . & . \end{pmatrix} & \begin{pmatrix} 1 & . \\ . & . \end{pmatrix} \end{pmatrix} \quad 31$$

Now our gradient of the cost function is

$$\frac{d}{dx} \left(\frac{1}{\lambda_p} \int_0^{\lambda_p} \text{Re} \left\{ \frac{\Delta \varepsilon_r}{\Delta \vec{\phi}} \right\} \text{d}x \right) = \text{cost G grad with x} \quad 32$$

Plugging in our fields and comparing to Eq. [\[full cost function def\]](#), we see that our derivative, and hence gradient calculation, is then

$$\frac{d}{dx} \left(\frac{1}{\lambda_p} \int_0^{\lambda_p} \text{Re} \left\{ \frac{\Delta \varepsilon_r}{\Delta \vec{\phi}} \right\} \text{d}x \right) = \frac{1}{\lambda_p} \int_0^{\lambda_p} \text{Re} \left\{ \frac{\Delta \varepsilon_r}{\Delta \vec{\phi}} \right\} \text{d}x \quad 33$$

Extending to the multi-pillar case is simply a matter of differentiating Eq. [\[multi pillar cost function\]](#) with Eq. [\[gradient calculation\]](#) as the single cell gradient.

$$\frac{d}{dx} \left(\frac{1}{\lambda_p} \int_0^{\lambda_p} \text{Re} \left\{ \frac{\Delta \varepsilon_r}{\Delta \vec{\phi}} \right\} \text{d}x \right) = -2 \frac{k_l^2}{\lambda_p} \text{Re} \left\{ \frac{\Delta \varepsilon_r}{\Delta \vec{\phi}} \right\} \quad 34$$

$$\frac{d}{dx} \left(\frac{1}{\lambda_p} \int_0^{\lambda_p} \text{Re} \left\{ \frac{\Delta \varepsilon_r}{\Delta \vec{\phi}} \right\} \text{d}x \right) = 2 \sum_n (G_n - d_n) \frac{d}{dx} \left(\frac{1}{\lambda_p} \int_0^{\lambda_p} \text{Re} \left\{ \frac{\Delta \varepsilon_r}{\Delta \vec{\phi}} \right\} \text{d}x \right) \quad 35$$

4. Non-Periodic Structures

Conventional particle accelerators must follow a synchronicity condition between the particle's motion and the oscillation of the accelerating field. This synchronization depends on particle velocity, cell length, types of confining field, and the frequency of the accelerating field. Different types of accelerators have different synchronicity conditions, but they all follow the same principle of matching the phase of the particle motion, to the applied fields. The grating wave-vector must be proportional to the in plane projection of the

incident laser's wave-vector, to achieve net acceleration $\lambda_p = m \cdot \beta \cdot \lambda$. Here we define λ_p as the periodicity of the structure (cell size), λ is the wavelength of the incident laser, and m is the diffraction order.

Since these are accelerating structures, the velocity of the particles will change. This change means that our synchronicity, is actually a function of time.

$$\lambda_p(t) = \beta(t) \cdot \lambda$$

Therefore, in a structure with a constant periodicity, the particle will gradually fall more and more out of phase with the applied field. We can calculate the maximum length of an acceleration structure, to just before the particle falls so far out of phase that it begins to experience a net deceleration. This maximum "dephasing" length is calculated to be

$$y_{\text{deph}} = \sqrt{\frac{\beta \lambda E_{\text{kin}} \left(\frac{E_{\text{kin}}}{m_0 c^2} + 1 \right) \left(\frac{E_{\text{kin}}}{m_0 c^2} + 2 \right)}{4 G_{\text{max}}(y_0)}} \quad 36$$

A quick back-of-the-envelope calculation for an electron, with injection velocity $\beta c = 0.4c$ and an incident laser wavelength $\lambda = 2\mu\text{m}$, gives us a maximum dephasing length on the order of a micron. This length is barely more than the synchronicity condition, thus we only get about one grating period of acceleration, drastically limiting their applications as accelerators. This is why we must introduce non-periodic acceleration structures which account for the particle acceleration and subsequent dephasing by sequentially adapting the size of each 'cell' of the structure to the phase velocity of the particle.

To find the energy gain of the particle, we integrate the Lorentz force over the distance it is applied ($\int F dy = Pt \rightarrow (Pt_2 - Pt_1) = W_2 - W_1 = \Delta W$), then

$$\begin{aligned} \Delta W(x, y; s) &= q \int_{-\lambda_p/2}^{\lambda_p/2} E_y(x, y; t = (y + s)/v) dy \\ &= q \int_{-\lambda_p/2}^{\lambda_p/2} \Re E_y(x, y) e^{i\omega_L(y+s)/v} dy \end{aligned} \quad 37$$

The variable s denotes the relative position of the particle behind an arbitrarily defined reference particle moving at $y = vt$.

Since we can control the phase of the particle's injection into the structure, we can control our arbitrary particle's position s relative to the field's phase with the adjoint source phase ϕ_{adj} . Unless otherwise noted, the particle was set to be in-phase with the field, hence the \cos term is 1 and our acceleration calculation used, for each cell in our simulations, was

$$\Delta W_n = q\lambda_{p_n} \Re e_{1_n} \cdot e^{i2\pi\lambda_{p_n}/\beta_n(\vec{r})\lambda} \quad 38$$

where the subscript n is used to denote the cell number. In order to make $\lambda_p \rightarrow \lambda_p(\vec{r})$, we see from Eq. [\[time dependent synchronicity\]](#) (note: we convert from $\beta(t) \rightarrow \beta(\vec{r})$ with the linear relation $\vec{r}(t) = \vec{v}(t)t$ that we need to find $\beta(\vec{r})$. Well, we know $\beta(r_0)$ because that is simply the injection energy of the particle, but to find the velocity at a later time, given the change in energy, we must use the function of energy

$$W_{n+1} = W_n + \Delta W_n \quad 39$$

here we work with the discrete cells labeled by n .

5. Methods

5.1. Custom Optimization Algorithm

For our optimization algorithm, first the user sets global constants like the laser wavelength, particle injection energy, etc. Then, the user creates their desired design curve. The design curve has to correlate to a property of the field harmonic (e_1), whether that be the magnitude or phase or a related quantity like the energy. Ultimately, if not the magnitude or phase of (e_1), the curve must be transformed to one of those quantities because of how we defined our cost function in Eq. [\[cost function definition\]](#). In a non-periodic structure, higher (e_1) values are possible at higher β (and thus larger λ_p). This dependence of the maximum $|e_1|$ on λ_p is quite complicated and analytically beyond the scope of this paper. Finding the maximum can be done numerically, though, after which, values can be scaled accordingly.

The optimizer runs a set number of calls to the objective function which returns G_n and ∂_{G_n} (from Eqs. [\[cost function definition\]](#) and [\[gradient calculation\]](#), respectively). The user sets a predefined step size κ and the optimizer steps around the parameter space.

We simulate the full forward field, but since we seek to optimize the first spatial harmonic, we must perform the Fourier transform. We want the first non-DC spatial harmonic, hence we select $e_{m=1}$ which nicely matches our previous notation. This is a complex-valued function and Fourier series coefficients are bounded by 1. Since this would indicate a single frequency source, but we use a dual drive system in this paper, the returned e_1 value must be divided in half to retain the normalization of the Fourier series.

With the adjoint phase defined as the phase between the incident laser and the particle's velocity, and we typically want the particle injected perfectly in phase with the laser, this

value should be set to $-\phi_{e_{1_1}}$ (i.e. minus the phase of the first harmonic of the first cell) to maximize the cos in Eq. [\[cost function definition\]](#). Due to the interference and edge effects of the ends of a non-periodic (any non-infinitely long) structure, in these simulations, the first several periods were essentially 'ignored' and the injection phase (adjoint phase) was set to the phase of a later period (generally $e_{1_{15}}$). This is a reasonable approximation to make because once the optimization of the end of the structure is implemented, in future work, the end of the structure can be matched to the interior cells, thereby not changing the validity of the results on the interior of the structure. From Eq. [\[cost function definition\]](#), we use $\phi_{e_1} = \arctan\left(\frac{\Re e_1}{\Im e_1}\right)$ to define our phase.

We see that the adjoint source envelope is spatially varying; however, in an accelerating structure, the periodicity is now also a function of position $\lambda_p(y)$. The acceleration was approximated as being at instantaneous intervals of the cell edges. The phase then is calculated for each cell's given periodicity. This produces multiple, discontinuous sinusoids of increasing frequency (due to increased velocity and thus λ_p). The discontinuities are dealt with by simply concatenating them. Producing, in effect, an exponential with a discretely changing frequency at the ends of each cell. Once particle tracking is added to the algorithm, this phase can be made pseudo-continuous by calculating the phase and periodicity at each grid point in the simulation region. It should be noted here, that because we assume no dephasing within the cells, we are not required to run the adjoint simulation, saving computation time. In Eq. [\[gradient calculation\]](#), the forward and adjoint fields cancel each other out, leaving only e_1 , $e^{i\phi_{adj}}$, and $\frac{\Delta \epsilon_r}{\Delta \phi}$. If we calculate the intra-periodic dephasing, then the fields will not cancel and the gradient calculation will again require both the forward and adjoint simulations.

To construct the $\frac{\Delta \epsilon_r}{\Delta \phi}$ matrix, we need to increment each parameter, individually, for the whole structure. In our case, our free parameters are the x-radius (r_x) and y-radius (r_y) of our pillars, and the y-position (y) of each pillar within its cell—here we define the y-position of the pillar by its axial center. So, we 'step' in r_x for the first cell, replace the pillar with the incremented parameter, record its relative permittivity array of ($\epsilon_{r_{j=0}}$), delete the pillar, reset the parameters, step in r_y for cell 1, and so on, collecting each ϵ_{r_j} for every parameter for every cell in the structure ($j = 0, 1, 2, \dots, N$), N being the length of our parameter vector $\vec{\phi}$. This gives

an epsilon array with respect to each parameter. We simply subtract each array, $\epsilon_{r_j} - \epsilon_{r_0}$, which is then ‘block-diagonalized’ by separating the arrays based on the periodicity of the structure and applying the filter based on (y) .

Our problem involves the imposition of bounds and constraints. Although there have been amazing strides made in the nano-fabrication industry, there are still fabrication and material constraints. For example, one of the constraints that we are limited by is the fabrication resolution—referring to the smallest feature size that can be successfully constructed. In our case, this was set to be 10nm. While you would ideally like to be able to make all of your steps in discrete steps of exactly 10nm, unfortunately, this is not how our gradient is calculated and imposing such a constraint is a non-trivial matter. Ref. provides a possible solution to this problem in the form of level-set parameterizations, which can be used to define a discrete structure.

Typical gradient based optimization applies bounds and constraints after the gradient has been calculated. If the elements of the Jacobian are independent of each other, this is not an issue, but in our case where they are not independent, our step in parameter space will be skewed, thus not moving us in the direction of the minimum because the gradient is calculated for the entire parameter space and cannot be modified *ex post facto*. This means the only place we can add bounds and constraints without losing information is during the construction of $\frac{\Delta\epsilon_r}{\Delta\phi}$. In practice this was accomplished by constraining the ‘step’ used to increment each parameter in the construction of the delta epsilon matrix.

Another reason why it is not feasible to alter the gradient after it has been calculated, is that our system has a non-convex parameter space. In a convex parameter space, there is one global minimum and the gradient is consistently and strongly in the direction of that global minimum (e.g. a parabola). In a non-convex parameter space, though, there are many local extrema and so any skew to your gradient may cause you to traverse out of a minima.

To efficiently traverse this non-convex parameter space, we employ a basin-hopping algorithm, outside of the main optimizer. This two part method uses a global stochastic stepping algorithm to randomly step around the parameter space. Each one of these ‘basins’ that the global algorithm starts in, is locally minimized. Then, the lowest minimum is then taken as the global minimum. The concept was originally designed to mimic the natural process of energy minimization of clusters of atoms [34].

Another complication that our algorithm has to account for is the structure’s non-periodicity. With non-periodic structures we lose our periodic boundary conditions and therefore have to adjust our original model of a plane wave impinging upon a semi-infinite periodic structure. In principle we still assume a plane wave-front, however, we no longer have an infinitely periodic structure; meaning, there will be unwanted diffraction at the ends of the structure. At the edges we see waves that propagate parallel to the grating causing interference, colloquially known as ‘edge effects.’ These effects are described semi-classically as originating from a delta-function point source, which we approximate as a Gaussian filter with a variance of λ . In simulation terms, these are often called transient sources. For our optimizations, we simply ignore the first and last few periods, set the injection phase to that of first non-interference cell, and apply the Gaussian filter in our adjoint method modifications.

6. Simulations

All simulations were done with an incident laser with $\lambda = 1.932\mu\text{m}$. For our calculation of ΔW , we used a field intensity of $\Re e_1 \cdot 100 \text{ MV/m}$. Since the function used for the constraints allows for a small step outside of them, they should be set just inside of the hard bounds. Our constraints on the system were the minimum radius size ($r_{x_{\min}}$ and $r_{y_{\min}}$), maximum radius size ($r_{x_{\max}}$ and $r_{y_{\max}}$), change in radii between neighboring cells (Δr_x and Δr_y), minimum y -position within its cell (y_{\min}), and maximum y -position (y_{\max}). These constraints primarily come from the damage threshold and fabrication limitations. Here we define a ‘normalized’ $(0-1) e_1$ value as $\Re \frac{e_1}{2 \cdot 100 \text{ MV/m}}$, where we account for the dual drive laser power to regain our normalization of the Fourier coefficient. Lastly, to deal with the transient interference from the structure ends, we used a temporal apodization in our simulations. Since our particle will only take tens of femtoseconds to traverse a cell, it is reasonable to use an apodization filter with an FWHM of 60 fs (chosen as it reduces noise without losing useful information).

Global Bounds and Constraints

	Constraints	Bounds
$r_{x_{\min}}$	$\frac{\lambda_{p_n}}{2} \cdot 0.25$	100 nm
$r_{y_{\min}}$	$\frac{\lambda_{p_n}}{2} \cdot 0.25$	100 nm
y_{\min}	$\lambda_{p_n} \cdot 0.25$	$\lambda_{p_{n-1}} + r_y$
$r_{x_{\max}}$	$\frac{\lambda_{p_n}}{2} \cdot 0.75$	$\frac{\lambda_{p_n}}{2} \cdot 0.9$

	Constraints	Bounds
$r_{y\max}$	$\frac{\lambda_{pn}}{2} \cdot 0.75$	$\frac{\lambda_{pn}}{2} \cdot 0.9$
y_{\max}	$\lambda_{pn} \cdot 0.75$	$\lambda_{pn} - r_y$
Δr_x	20 nm	N/A
Δr_y	20 nm	N/A
[global bounds and constraints]		

7. Results

7.1. Parameter Space Map

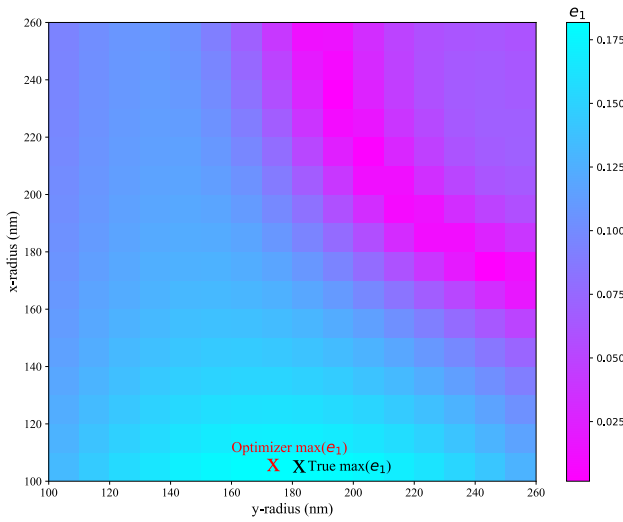


Figure 4.1: **Parameter Space Map.** Brute force map of the parameter space for a single cell in an infinitely periodic structure with an injection energy of 30.30 keV. This mapping was done with the radius of the major and minor axis of an ellipsoid pillar as the parameters. The steps in the mapping were set at our fabrication resolution of 10 nm. The maximum possible $\text{Re}\{e_1\}$ value was found at $r_x = 100$ nm and $r_y = 170$ nm, while the optimizer converged at $r_x = 100$ nm and $r_y = 160$ nm, which is within the convergence tolerance of the optimizer.

The first step was to test the optimizer. To do this, we did a brute force mapping of the parameter space, for a single configuration, and then ran the optimizer to see if it converged to the same minimum. For the brute force mapping, we set the adjoint phase to $-\phi_{e_1}$ in order to maximize $\text{Re}_1 \cdot e^{i\phi_{\text{adj}}}$. Fig. 4.1 shows the parameter space for a single cell of an infinitely periodic structure. This mapping was done with the radius of the major and minor axis of an ellipsoid pillar as the

parameters (r_x and r_y). The steps in the mapping were set at our fabrication resolution of 10 nm. The maximum possible Re_1 value was found at $r_x = 100$ nm and $r_y = 170$ nm, while the optimizer converged at $r_x = 100$ nm and $r_y = 160$ nm. Although the optimizer did not find the true global maximum, it can be seen from the figure that the difference between the points is nearly indistinguishable, hence, the optimizer did successfully find the true maximum within its convergence tolerance.

7.2. Dynamic y-position Parameter

Next, we wanted to test the effect of the y-position on e_1 . In Fig. 4.2, the magnitude of e_1 never changes by more than 1%. We do see, however, that the phase of e_1 changes as the pillar moves within its cell, as expected. Both Fig. 4.2 and 4.3 show that we are able to get a nearly 180° phase shift from moving the pillar from the bottom of its cell to the top (*bottom* being closer to $y = 0$, *top* being further from $y = 0$ in our coordinate system).

This is a vital parameter to be able to control, especially for non-periodic structures, because the purpose of having the increasing cell size is to maintain the field phase with that of the particle's trajectory. Having an optimizable y-position parameter, thus, allows greater control over the phase of e_1 and lets us maintain a greater level of synchronicity to avoid unwanted dephasing. It should be noted, though, that the level of control and the range of phase angle available is not necessarily as good as is shown in the aforementioned plot. This is due to the interaction between cells and their effects on each other, since, in a real structure, it is not an infinitely periodic object.

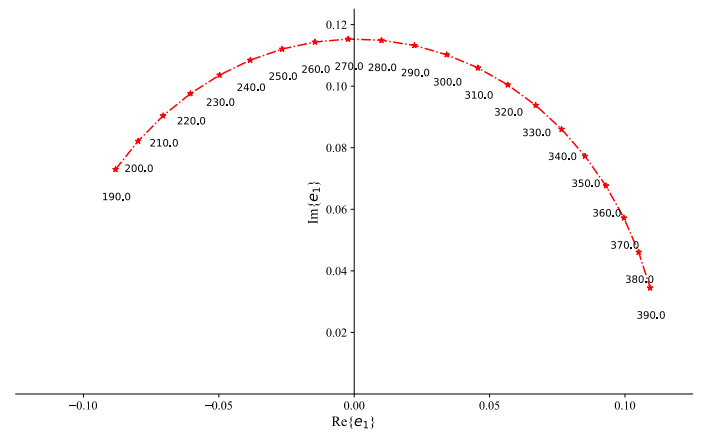


Figure 4.2: Complex e_1 phase plot. The figure shows the phase of e_1 , in terms of its real and imaginary parts,

as the single-cell, infinitely periodic structure had its pillar shifted along the y-axis in its cell.

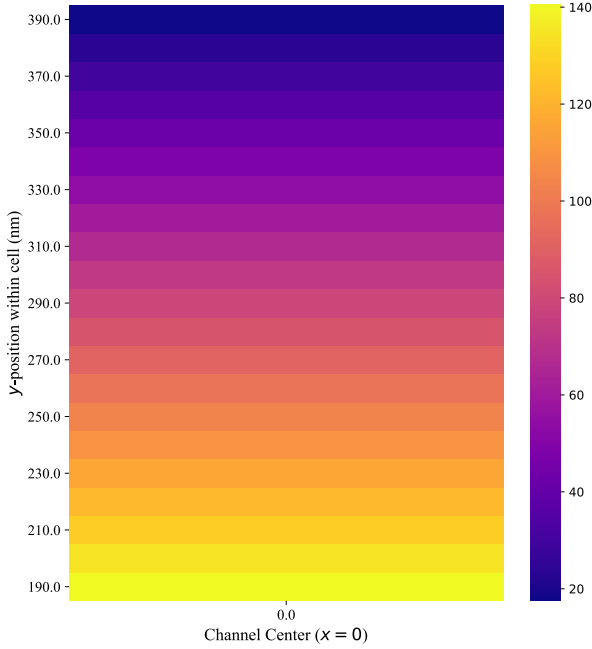


Figure 4.3: Angular Phase of e_1 Plot. As the pillar is moved from the bottom to the top of the cell, the phase of e_1 changes nearly 180 degrees. The phase of e_1 is calculated as the $\arctan(\text{Re}/\text{Im})$, at the channel center ($x=0$). This shows that the y-position of the pillars within their cell strongly influences the phase of e_1 .

7.3. Non-Periodic Structure Optimization

We attempted to make the periodicity into a dynamic, optimizable parameter, but this proved to be beyond the scope of this paper. The primary difficulty lies in the link between e_1 , β , and λ_p . To expound, β_{n+1} is determined by the product $e_{1n} \cdot \lambda_{pn}$, while $\lambda_{p_{n+1}}$ is then determined by β_{n+1} . We see that for every change in e_{1n} , there will necessarily need to be a change in $\lambda_{p_{n+1}}$. Similarly, every change in λ_{pn} will cause a change in $\lambda_{p_{n+1}}$. However, if there is no change in $\lambda_{p_{n+1}}$, this will necessarily change $e_{1_{n+1}}$ from the previous iteration. Conceptually this leads to the optimizer being a ‘step behind’ itself—changing λ_p based on the previous iteration which is not accurate to the current structure’s parameters.

$$\lambda_{p_{n+1}} \propto \beta_{n+1} \propto e_{1n} \cdot \lambda_{pn}$$

Another implementation was to update $\lambda_{p_{n+1}}$ progressively. Since β_{n+1} depends on λ_{pn} though, and the

adjoint source is supposed to mimic the particle phase velocity, we would have to run a forward and adjoint simulation for the incrementing of each cell. Conceptually, if we run a forward and adjoint simulation, then increment the periodicity of period 1, now β_{n+1} is different and this is propagated down the structure due to the recursive-like relationship between β , λ_p , and e_1 . Hence, we would need to run forward and adjoint simulations for the incrementing of each successive period. For large structures, it is easy to see that this begins to defeat the purpose of the adjoint method because you are requiring many time-consuming and computationally expensive simulations. For these reasons, it was chosen here to define the periodicity based on the ideal case, here the input design curve, d_n . This method allows the adjoint source to be set as a facsimile of the desired particle trajectory. This resolves the issue mentioned above about having the optimizer being a step behind the adjoint source, since it remains the same for every iteration. This also maintains the 2-simulation requirement from the adjoint method.

7.4. Non-Periodic Sinusoid Optimization

Simulation Parameters

β	0.35
Injection energy W	34.50 keV
Number of periods	300
First and last periods ignored	15
Structure length	204.84 μm

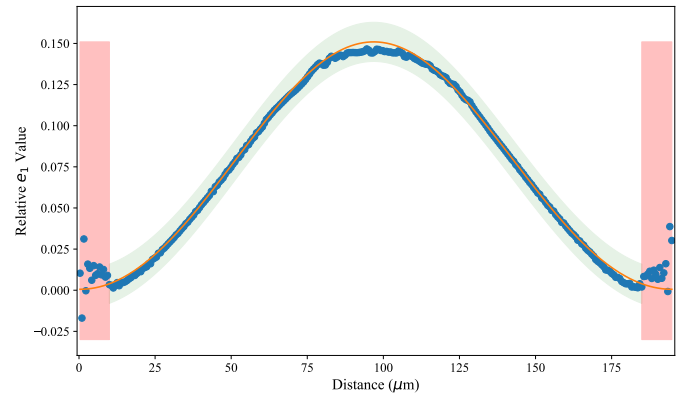


Figure 4.4: Non-Periodic Sinusoid Optimization. A sinusoid design curve of e_1 values was optimized for, in a non-periodic structure. The orange line is the desired design curve, the blue dots are the e_1 values of each cell, the green shaded region is the convergence tolerance of the optimizer, and the red shaded region on the ends are the ‘ignored’ cells on the ends of the structure.

To test the flexibility of the optimizer, 3 progressively more complicated design curves were created and set for non-periodic structures. The shaded region is calculated from the maximum possible $\Re e_1$ value at the given *injection* energy. Typically, we might use a normal percentage as our metric by which to judge the optimization. However, since only a portion of the field energy is available for us to utilize, it makes more sense to use the maximum possible $\Re e_1$ to set our scale. Here we use an interval, extended 5% beyond the design curve, as our tolerance. This visually shows us where we are within 5% of the design curve, hence, within this green band values match the design curve by 95% +. Fig. 4.4 shows the optimization result of a non-periodic structure with a sinusoidal design curve, similar to that shown in Fig. [periodic multicell optimization] and [nonperiodic multicell optimization]. This was done as a check of the validity of the optimization. Since we knew it could successfully converge on sinusoidal design curves for small scale structures (both periodic and non-periodic), we needed to verify that the algorithm could be easily scaled to larger structures. As we can see in the figure, the algorithm was very successful at matching the design curve within the tolerance (and the constraints). This structure is 300 periods (204.84 μm) and will accelerate our particle from 34.50 keV to 36.01 keV.

7.5. Superposition and Sawtooth Curves

Superposition Parameters		Sawtooth Parameters	
β	0.4	β	0.35
Injection	46.55	Injection	34.50
energy W	keV	energy W	keV
Number of	150	Number of	150
periods		periods	
First and	10	First and	15
last periods		last periods	
ignored		ignored	
Structure	116.23	Structure	101.84
length	μm	length	μm

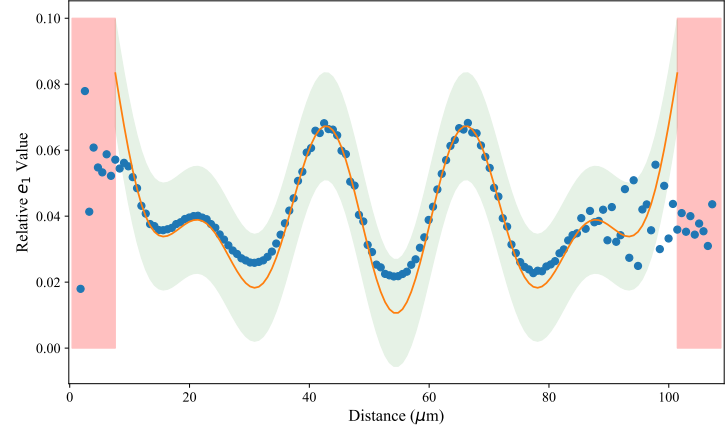


Figure 4.5: Superposition Sinusoid Optimization. A non-periodic structure with multiple sinusoids superimposed to generate the design curve. The orange line is the desired design curve, the blue dots are the e_1 values of each cell, the green shaded region is the convergence tolerance of the optimizer, and the red shaded region on the ends are the ‘ignored’ cells on the ends of the structure.

If the algorithm can find structures that could match various sinusoidal design curves, it begged the question, could it match a combination of sinusoids? That is, could we use a super position of sine waves to make arbitrarily complicated design curves? Yes, and No—arbitrary up to a point. Fig. 4.5 shows that the optimizer was quite good at matching a superposition design curve (minus some outliers further towards the outside of the structure). It should be noted, that this curve was chosen with *a priori* knowledge. From experience with the simulations, there was a level of intuition about the limit to the complexity that the optimizer could successfully handle. This was tested more thoroughly in Fig. 4.6. From the tests with sawtooth wave design curves, it was found that the upper limit was a change of $\Re e_1 \approx 0.1/10$ periods. Fig. 4.6 shows that the optimizer is still very accurate up to this limit, however, much beyond this rate of change in $\Re e_1$ and the optimizer will tend to ‘run away.’ This is true for any design curve that is not physically possible, therefore more development is needed to keep the optimizer as close to the best, physically possible, solution, without running away, chasing a possibly unobtainable design curve.

One major limiting factor is our fabrication constraint of a change in neighboring pillars parameters Δr_x and Δr_y not being able to exceed 20 nm. With this system, though, we can, in theory, optimize for arbitrarily complicated design curves up to this limit. This is an exciting result as it shows that we

can have great control over the particle as it traverses the structure, providing huge flexibility in the functionality of the accelerator.

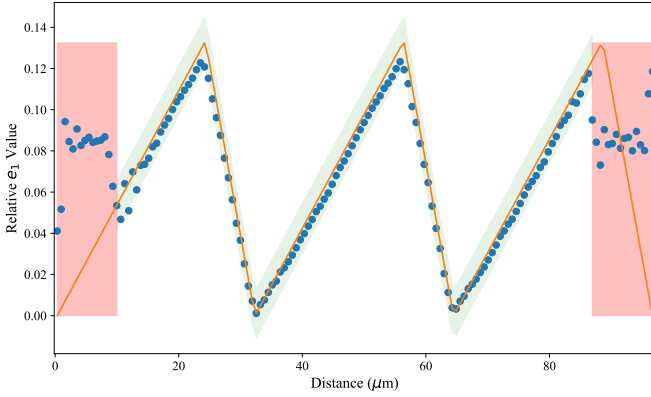


Figure 4.6: Superposition Sinusoid Optimization. A non-periodic structure with a sawtooth design curve was optimized. This kind of curve demonstrates the maximum rate of change of $\text{Re}\{e_1\}$ between cells. The orange line is the desired design curve, the blue dots are the e_1 values of each cell, the green shaded region is the convergence tolerance of the optimizer, and the red shaded region on the ends are the ‘ignored’ cells on the ends of the structure.

8. Conclusion

As we have seen, the adjoint method cannot be directly applied to our dual pillar photonic structure due to the asymmetry of the parameter space. However, with some mathematical tricks, we can modify the adjoint method and account for the intra- and inter-cell interactions. In doing so, we restore a level of ‘block-diagonality’ to our adjoint calculations—necessary for the algebraic relations used in the adjoint method. The adjoint method provides us an orders-of-magnitude improvement on simulation efficiency by requiring only 2-simulations per iteration to calculate the gradient (rather than $N = \text{the number of parameters} + 1$).

Our modification to the adjoint method accounts for non-periodic conditions through the inter-period interactions. By using a Gaussian filter, calculated by y -distance, we can symmetrize our permittivity matrix even for non-periodic structures. Non-periodic structures being of interest due to the dephasing that occurs with an accelerating particle and the laser field. Our custom optimization algorithm applies a modified adjoint method and modified adam algorithm while imposing bounds and constraints. The optimizer was successful at matching complicated design curves to 95+% accuracy, up to a rate of change in e_1 of 0.1/10 periods.

As discussed in Sec. 2.2, a periodic structure, with a 100 MeV/m field gradient, could only provide a net energy gain of 100 eV, whereas we have shown that non-periodic structures can provide, ≈ 1.5 keV (in a 200 micron structure, without dephasing, yet). With currently demonstrable field gradients of 10 GeV/m, we can expect structures with up to 7.5 MeV gain in 3 mm. These accelerations are nearly 200x larger than SLAC (0.038 MeV) while being nearly 20x smaller (5.25 cm). This is exciting for future research as it opens the doors to scaled down accelerators, 3 orders of magnitude smaller than current linacs. Miniaturization of particle accelerators provides new opportunities for novel applications of the technology. The level of control offered by modified adjoint inverse design also brings the benefit of flexibility beyond that of a typical linac.

9. Future Considerations

The optimization algorithm was written in such a way that it balances robustness with flexibility, to allow additions and modifications to be made. Our algorithm, then, aims to be a basis for the next steps in this research. This includes optimization of structure ends, implementation of particle tracking, optimizable pillar angle, extension to broadband light, and inclusion of level-set functions.

Optimization of the structure ends would require a different cost function, so the ends of the structure would have to be separately optimized then added as a constant/fixed structure, to the optimization simulations of the central majority of the structure. Implementing particle tracking software with this optimization algorithm would be able to account for the particle’s true phase, even as it traverses the individual cells.

In our simulations, we used monochromatic lasers and they were modeled as a plane wave. Since real DLA structures require the high peak field intensities of ultra-short laser pulses—from the uncertainty principal—we know this means that the beam necessarily is not monochromatic. The next step, then, would involve generalizing our method for broadband light. This will involve optimizing harmonics of the different wavelengths in the pulse carrier envelope.

As was detailed in section [Constrained Optimization], in a real structure, we are bound by fabrication constraints. While it is relatively straightforward to impose our boundary constraints, it is non-trivial to make the optimizer use step sizes that correspond directly to our fabrication resolution (here 10 nm). Ref. provides a way of using, so-called, *level-set functions* to impose these kinds of step function constraints. For example, in our simulations, the optimizer

would converge and have values such as 173.6 nm \times 198.1 nm. Where, due to our fabrication resolution constraints, the closest we could get to that would be 170 nm \times 200 nm. However, given the complexity of the parameter space, this may not always be the best solution (e.g. perhaps the minimum is 173.6 nm \times 198.1 nm, but the second best, fabricable structure might be 180 nm \times 190 nm). Hence the need for some development on these kinds of constraints within this optimizer.

We also note that although the periodicity was not made into a dynamic parameter, as detailed in a previous section, it could still be possible to devise a clever way to implement the periodicity as an optimizable parameter.

10. Acknowledgements

Proin pharetra nonummy pede. Mauris et orci. Aenean nec lorem. In porttitor. Donec laoreet nonummy augue. Suspendisse dui purus, scelerisque at, vulputate vitae, pretium mattis, nunc. Mauris eget neque at sem venenatis eleifend. Ut nonummy.

11. References

- [1] Tyler Hughes, Georgios Veronis, Kent P. Wootton, R. Joel England, and Shanhui Fan. Method for computationally efficient design of dielectric laser accelerator structures. *Opt. Express*, 25(13):15414, June 2017.
- [2] Christopher M. Lalau-Keraly, Samarth Bhargava, Owen D. Miller, and Eli Yablonovitch. Adjoint shape optimization applied to electromagnetic design. *Opt. Express*, 21(18):21693, September 2013.
- [3] Armand C. R. Niederberger, David A. Fattal, Nicolas R. Gauger, Shanhui Fan, and Raymond G. Beausoleil. Sensitivity analysis and optimization of sub-wavelength optical gratings using adjoints. *Opt. Express*, 22(11):12971, June 2014.
- [4] Tyler W. Hughes, Momchil Minkov, Ian A. D. Williamson, and Shanhui Fan. Adjoint Method and Inverse Design for Nonlinear Nanophotonic Devices. *ACS Photonics*, 5(12):4781–4787, December 2018.
- [5] Tyler W. Hughes, Si Tan, Zhixin Zhao, Neil V. Saprà, Yun Jo Lee, Kenneth J. Leedle, Huiyang Deng, Yu Miao, Dylan S. Black, Minghao Qi, Olav Solgaard, James S. Harris, Jelena Vuckovic, Robert L. Byer, and Shanhui Fan. On-Chip Laser Power Delivery System for Dielectric Laser Accelerators. *Phys. Rev. Applied*, 9(5):054017, May 2018. arXiv:1709.04441 [physics].
- [6] J. Vuckovic. Inverse designed on-chip laser driven particle accelerator, October 2020.
- [7] Sami G Tantawi, Valery Dolgashev, Aaron Jansen, Michael Fazio, Mark Kemp, Jeff Neilson, and Zenghai Li. High Gradient RF Acceleration at SLAC. page 16.
- [8] SLAC | laboratory, Menlo Park, California, United States | Britannica.
- [9] Helmut Wiedemann. Particle Accelerator Physics. Advanced Texts in Physics. Springer, Berlin, Heidelberg, 2003.
- [10] M. Kozák, N. Schöonenberger, and P. Hommelhoff. Ponderomotive Generation and Detection of Attosecond Free-Electron Pulse Trains. *Phys. Rev. Lett.*, 120(10):103203, March 2018.
- [11] D. Cesar, S. Custodio, J. Maxson, P. Musumeci, X. Shen, E. Threlkeld, R. J. England, A. Hanuka, I. V. Makasyuk, E. A. Peralta, K. P. Wootton, and Z. Wu. High-field nonlinear optical response and phase control in a dielectric laser accelerator. *Commun Phys*, 1(1):1–7, August 2018. Number: 1 Publisher: Nature Publishing Group.
- [12] Kenneth J. Leedle, Dylan S. Black, Yu Miao, Karel E. Urbanek, Andrew Ceballos, Huiyang Deng, James S. Harris, Olav Solgaard, and Robert L. Byer. Phase-dependent laser acceleration of electrons with symmetrically driven silicon dual pillar gratings. *Opt. Lett.*, OL, 43(9):2181–2184, May 2018. Publisher: Optica Publishing Group.
- [13] Joshua McNeur, Martin Kozák, Norbert Schöonenberger, Kenneth J. Leedle, Huiyang Deng, Andrew Ceballos, Heinar Hoogland, Axel Ruehl, Ingmar Hartl, Ronald Holzwarth, Olav Solgaard, James S. Harris, Robert L. Byer, and Peter Hommelhoff. Elements of a dielectric laser accelerator. *Optica*, OPTICA, 5(6):687–690, June 2018. Publisher: Optica Publishing Group.
- [14] A. W. Lohmann. Particle accelerator utilizing coherent light.
- [15] K. Mizuno, J. Pae, T. Nozokido, and K. Furuya. Experimental evidence of the inverse Smith–Purcell effect. *Nature*,

- 328(6125):45–47, July 1987. Number: 6125 Publisher: Nature Publishing Group.
- [16] E. A. Peralta, K. Soong, R. J. England, E. R. Colby, Z. Wu, B. Montazeri, C. McGuinness, J. McNeur, K. J. Leedle, D. Walz, E. B. Sozer, B. Cowan, B. Schwartz, G. Travish, and R. L. Byer. Demonstration of electron acceleration in a laser-driven dielectric microstructure. *Nature*, 503(7474):91–94, November 2013. Number: 7474 Publisher: Nature Publishing Group.
- [17] N. Schonenberger and P. Hommelhoff. Dielectric Laser Acceleration, August 2020. arXiv:2008.03958 [physics].
- [18] C. Joshi. The Los Alamos Laser Acceleration of Particles Workshop and beginning of the advanced accelerator concepts field. *AIP Conference Proceedings*, 1507(1):61–66, December 2012. Publisher: American Institute of Physics.
- [19] R. Shiloh, T. Chlouba, P. Yousefi, and P. Hommelhoff. Particle acceleration using topilluminated nanophotonic dielectric structures. *Opt. Express*, OE, 29(10):14403–14411, May 2021. Publisher: Optica Publishing Group.
- [20] R. Joel England, Robert J. Noble, Karl Bane, David H. Dowell, Cho-Kuen Ng, James E. Spencer, Sami Tantawi, Ziran Wu, Robert L. Byer, Edgar Peralta, Ken Soong, ChiaMing Chang, Behnam Montazeri, Stephen J. Wolf, Benjamin Cowan, Jay Dawson, Wei Gai, Peter Hommelhoff, Yen-Chieh Huang, Chunguang Jing, Christopher McGuinness, Robert B. Palmer, Brian Naranjo, James Rosenzweig, Gil Travish, Amit Mizrahi, Levi Schachter, Christopher Sears, Gregory R. Werner, and Rodney B. Yoder. Dielectric laser accelerators. *Rev. Mod. Phys.*, 86(4):1337–1389, December 2014. Publisher: American Physical Society.
- [21] K. P. Wootton, J. McNeur, and K. J. Leedle. Dielectric Laser Accelerators: Designs, Experiments, and Applications. *Rev. Accel. Sci. Tech.*, 09:105–126, January 2016. Publisher: World Scientific Publishing Co.
- [22] Peyman Yousefi, Norbert Schonenberger, Joshua Mcneur, Martin Kozák, Uwe Niedermayer, and Peter Hommelhoff. Dielectric laser electron acceleration in a dual pillar grating with a distributed Bragg reflector. *Opt. Lett.*, OL, 44(6):1520–1523, March 2019. Publisher: Optica Publishing Group.
- [23] John Breuer and Peter Hommelhoff. Laser-based acceleration of non-relativistic electrons at a dielectric structure. *Phys. Rev. Lett.*, 111(13):134803, September 2013. arXiv:1308.0464 [physics].
- [24] Dylan S. Black, Zhixin Zhao, Kenneth J. Leedle, Yu Miao, Robert L. Byer, Shanhui Fan, and Olav Solgaard. Operating modes of dual-grating dielectric laser accelerators. *Phys. Rev. Accel. Beams*, 23(11):114001, November 2020. Publisher: American Physical Society.
- [25] Uwe Niedermayer, Thilo Egenolf, and Oliver Boine-Frankenheim. Beam dynamics analysis of dielectric laser acceleration using a fast 6D tracking scheme. *Phys. Rev. Accel. Beams*, 20(11):111302, November 2017. Publisher: American Physical Society.
- [26] T. Plettner, R. L. Byer, E. Colby, B. Cowan, C. M. S. Sears, J. E. Spencer, and R. H. Siemann. Visible-Laser Acceleration of Relativistic Electrons in a Semi-Infinite Vacuum. *Phys. Rev. Lett.*, 95(13):134801, September 2005. Publisher: American Physical Society.
- [27] Dries Vercruyse, Neil V. Sapra, Logan Su, Rahul Trivedi, and Jelena Vučković. Analytical level set fabrication constraints for inverse design. *Sci Rep*, 9(1):8999, June 2019. Number: 1 Publisher: Nature Publishing Group.
- [28] Understanding time apodization in frequency domain monitors.
- [29] J W Wang and G A Loew. MEASUREMENTS OF ULTIMATE ACCELERATING GRADIENTS IN THE SLAC DISK-LOADED STRUCTURE. page 17.